Remote Sensing **2010**, *2*, 1662-1679; doi:10.3390/rs2071662

OPEN ACCESS

Remote Sensing

ISSN 2072-4292

www.mdpi.com/journal/remotesensing

Article

Design and First Results of an UAV-Borne L-Band Radiometer for Multiple Monitoring Purposes

Rene Acevo-Herrera [1,*], Albert Aguasca [1], Xavier Bosch-Lluis [1,2], Adriano Camps [1,2], José Martínez-Fernández [3], Nilda Sánchez-Martín [3] and Carlos Pérez-Gutiérrez [3]

[1] Remote Sensing Lab, Department of Signal Theory and Communications, Universitat Politècnica de Catalunya, UPC Campus Nord D3, E-08034 Barcelona, Spain;
E-Mails: rene.acevo@tsc.upc.edu (R.A.-H.); aguasca@tsc.upc.edu (A.A.);
xavier.bosch@tsc.upc.edu (X.B.-L.); camps@tsc.upc.edu (A.C.)

[2] IEEC CRAE, UPC, Barcelona, Spain

[3] Centro Hispano-Luso de Investigaciones Agrarias (CIALE) Universidad de Salamanca, Parque Científico Campus de Villamayor C, Río Duero, 12, E-37185 Villamayor (Salamanca), Spain;
E-Mails: jmf@usal.es (J.M.-F.); nilda@usal.es (N.S.-M.); carpegu@usal.es (C.P.-G.)

* Author to whom correspondence should be addressed; E-Mail: rene.acevo@tsc.upc.edu;
Tel.: +34-934-017-362.

Received: 30 April 2010; in revised form: 15 June 2010 / Accepted: 22 June 2010 / Published: 29 June 2010

Abstract: UAV (unmanned Aerial Vehicle) platforms represent a challenging opportunity for the deployment of a number of remote sensors. These vehicles are a cost-effective option in front of manned aerial vehicles (planes and helicopters), are easy to deploy due to the short runways needed, and they allow users to meet the critical requirements of the spatial and temporal resolutions imposed by the instruments. L-band radiometers are an interesting option for obtaining soil moisture maps over local areas with relatively high spatial resolution for precision agriculture, coastal monitoring, estimation of the risk of fires, flood prevention, *etc.* This paper presents the design of a light-weight, airborne L-band radiometer for deployment in a small UAV, including the hardware and specific software developed for calibration, geo-referencing, and soil moisture retrieval. First results and soil moisture retrievals from different field experiments are presented.

Keywords: UAV; airborne sensors; radiometer; soil moisture

---

1. Introduction

The interest of the scientific community in the remote measurement of geophysical parameters, such as the soil moisture (SM) or the sea surface salinity (SSS), has increased in the last years and much effort has been spent developing research instruments. This has been done mainly by the European Space Agency (ESA), with the MIRAS/SMOS [1], and the National Aeronautics and Space Administration (NASA), with AQUARIUS/SAC-D [2,3] and SMAP [4] missions. These space-borne radiometers have been optimized to measure the aforementioned variables globally, at mesoscale resolution, with short revisit time (~3 days): pixel size is ~100 km for a 0.1 psu SSS accuracy, or the pixel size is ~50 km for a 4% SM accuracy. However, these systems are not adequate for regional or local applications, where higher resolution imagery is required. Airborne microwave radiometers flying at low altitudes can fulfill this lack of information; they can improve the spatial resolution up to tens of meters without virtually any revisit time restrictions. Furthermore, these platforms are less sensitive to atmospheric effects. The SLFMR aboard a Beaver de Havilland [5] and MIRAMAP's radiometers [6] are examples of airborne radiometers. In this context, small unmanned aerial vehicles (UAV) have been found to be the ideal platforms for this kind of remote sensing application [7], because they are easy to deploy, more flexible, and offer a high level of re-configurability.

This work describes a radiometer system that performs soil moisture mapping from low altitude small UAV platforms. The paper is organized as follows: Section 2 presents an introductory overview to the system. Section 3 analyzes the onboard airborne radiometer. The software processor is presented in Section 4; the processor focuses on radiometer calibration, data geo-referencing and representation, data interpolation, and SM retrieval algorithms. Section 5 is devoted to the analyses of soil moisture measurements. Finally, Section 6 summarizes the main conclusions of this paper.

2. System Description

There are a number of restrictions in the design process for a microwave radiometer and the platform. Assuming their use in precision farming, it is desired to have an absolute accuracy lower than ≈10 K to determine SM with errors lower than 4%. Additionally, a spatial resolution between 30 and 150 m, while flying at altitudes of up to 300 m, is desirable.

The use of UAV platforms to carry remote sensors imposes not only strong constraints on the size, weight, and power consumption of the sensors. Moreover, due to the strong vibrations of the UAV engine induces, an extra effort is required to increase the robustness of the instrument. These vibrations can reach more than 6 g for gasoline engine powered radio-controlled aircrafts, so that special care must be taken in the whole system design process.

The main parts of the system that are deployed in the UAV platform are: the L-band Radiometer, including the antenna, a Global Positioning System (GPS) receiver, an Inertial Motion Unit (GPS-IMU), and the datalogger. Different UAV platforms have been used, all of them with a 2.5 m wingspan and 2 m length (Figure 1).These UAVs are able to fly at altitudes of up to 400 m, with cruise speeds between 25-45 m/s and an endurance of up to 20 min, while carrying a payload of up to 3.5 kg.

The platform is provided with the GPS-IMU for the purpose of geo-referencing the collected radiometric data. The radiometer's output signal, the attitude (roll, pitch, and yaw), the altitude, and the

aircraft speed (v_x, v_y, and v_z) are properly recorded by the onboard data-loggers for later data processing at a sampling rate of 50 samples per second.

Figure 1. The UAV during a test flight. The ARIEL antenna is located below the fuselage.

3. Airborne L-band Radiometer

A single polarization nadir-looking Dicke radiometer was selected and implemented, due to its simplicity and sufficient stability when thermally stabilized. The system was designed to require external periodic calibration only at the beginning and end of each flight (≥20 min).

An important issue to take into account is the antenna. The antenna dimensions of the L-band are comparable to the size of the UAV itself if a narrow beamwidth is desired (e.g., less than 25° in both planes). Furthermore, the antenna has to be specifically designed in order to reduce its influence on the UAV aerodynamics, while preserving the desired performance for radiometric applications. The designed antenna (Figure 2a) is a flat hexagonal 7-patch array with a 22° beamwidth in both dimensions [8]. The measured gain, directivity, and radiation ohmic efficiency of this antenna are 15.88 dB, 16.03 dB, and 96.5%, respectively. The effect of the variation of antenna ohmic losses, which are due to temperature fluctuations, is minimized by incorporating a thermal control attached to antenna ground plane.

The Airborne RadIomEter at L-band (1.4 GHz) (ARIEL) block diagram is shown in Figure 3. The heterodyne receiver is divided into three main blocks: the RF front-end, the down-converter, and the detection block. The RF front-end (1,400 MHz to 1,427 MHz) includes the Dicke switch, which alternates the detected power between the signal from the antenna and from a matched load. This signal is properly filtered, amplified, and down-converted to a baseband, where it is detected using a true rms-detector (output voltage proportional to signal's standard deviation), followed by a square law amplifier. Finally, the signal is synchronously demodulated, low-pass filtered, and conditioned before the analog to digital conversion process.

Figure 2. (a) Setup for the antenna pattern measurement showing the antenna mounted on the UAV at the anechoic chamber of the Dept. of Signal Theory and Communications, Universitat Politècnica de Catalunya [9]. **(b)** Measured full radiation pattern. **(c)** Simulated and measured copolar radiation pattern at the E-plane. Simulation only considered ideal isotropic radiation elements, and thus, slight differences between simulated and measured results can be distinguished. **(d)** Measured cross-polar radiation pattern for the E-plane.

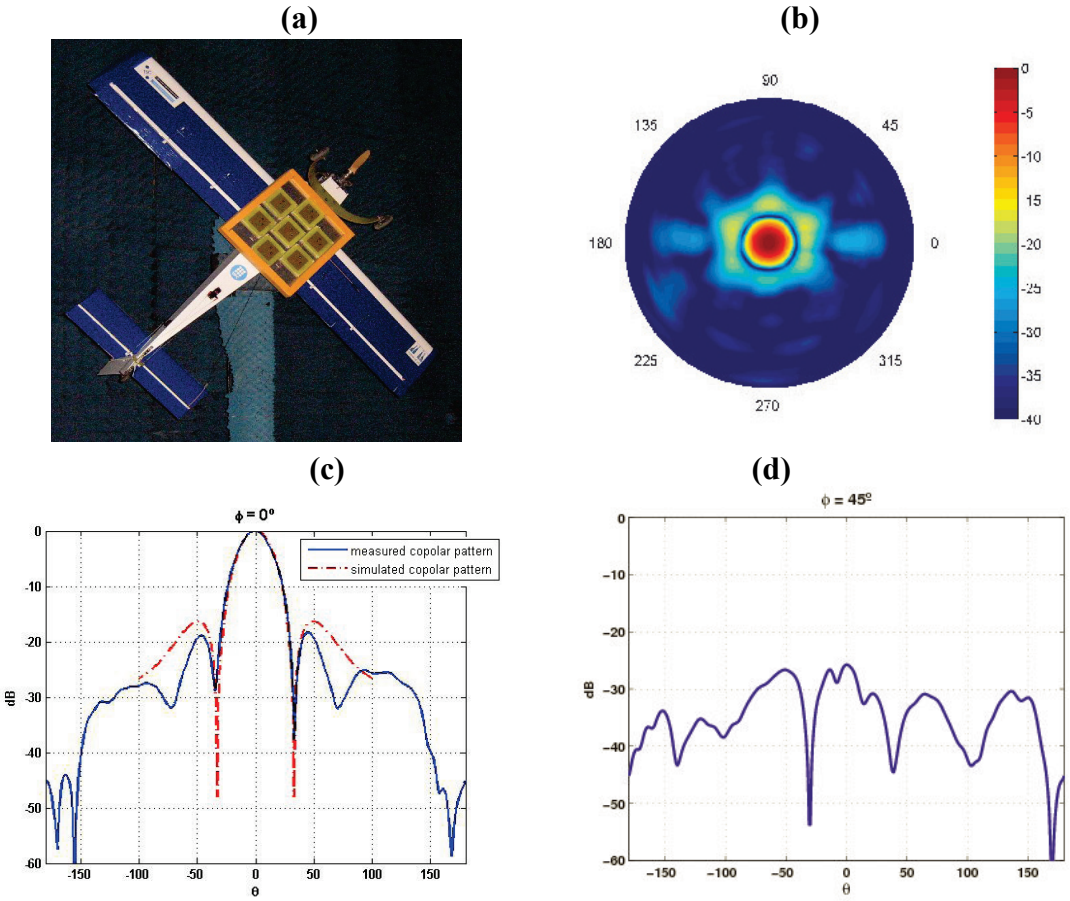

Figure 3. ARIEL block diagram.

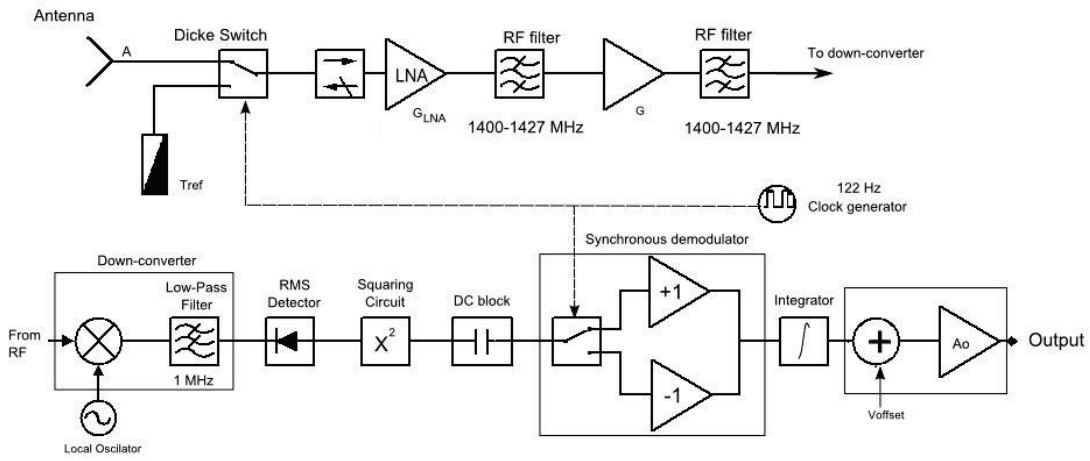

The radiometric sensitivity ΔT for a balanced Dicke radiometer is [10]:

$$\Delta T = \frac{2(T_{REF} + T_{REC})}{\sqrt{B\tau}}, \quad (1)$$

where T_{REF} = 315 K is the physical temperature of the reference load, $T_{REC} \approx$ 790 K is the receiver's noise temperature, $B \approx$ 30 MHz is the system's noise bandwidth, and τ is the integration time.

The maximum integration time is determined by the minimum dwell time according to,

$$\frac{FP_{\min}}{v_{\max}} = \frac{BW \times h_{\min}}{v_{\max}}, \quad (2)$$

where $FP_{\min}$ is the smallest footprint, BW is the antenna beamwidth, $h_{\min}$ is the minimum flight height, and $v_{\max}$ is the maximum flight speed. With these parameters, the theoretical radiometric resolution is ΔT = 1.27 K for an integration time of τ = 100 ms.

The radiometer was implemented using commercial "off-the-shelf" components. The radiometer front-end was integrated in a 100 × 60 × 15 mm monoblock box (Figure 4). The total weight, including the batteries, the antenna, and its radome, is less than 3 kg. If the thermal control of the radiometer is included, the total power consumption of the system is less than 10 W, which facilitates the use of light weight Lithium Polymer batteries as the main power supply.

Figure 4. ARIEL RF front end 100 × 60 × 20 mm compared to the size of a 1 euro coin.

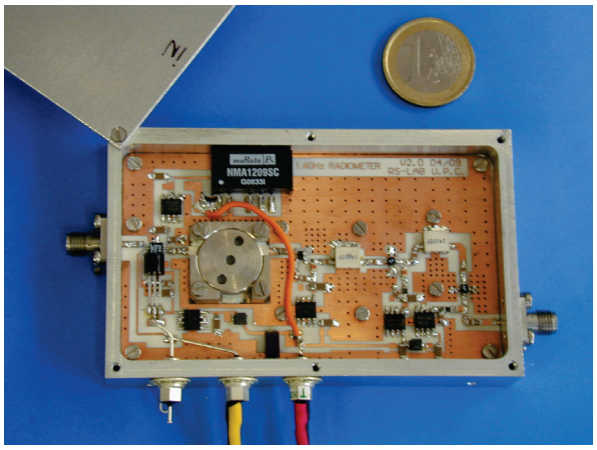

4. ARIEL Soil Moisture Retrieval Processor

A specific software processor for soil moisture retrieval has been developed to obtain soil moisture maps from the radiometric measurements. The input data files (GPS, IMU, attitude, and raw radiometric data) are selected from a specific graphical user interface (GUI), where the radiometric calibration procedure is defined. This radiometric data calibration procedure is performed before, after, or before and after the flight, according to an established protocol. Figure 5a shows this calibration process. The calibration is based on the selection of the intervals in the raw data where the hot or cold loads were measured.

Two independent dataloggers were used, one for the GPS, and the other for the inertial and radiometric data. To synchronize their data, cross-correlation techniques were used that applied the altitude information from GPS and the barometer (Figure 5b).

Figure 5. Data processing **(a)** Calibration of radiometer output (selection of calibration intervals), **(b)** Synchronization of the altitude data from GPS data and the barometric information data synchronization.

(a)

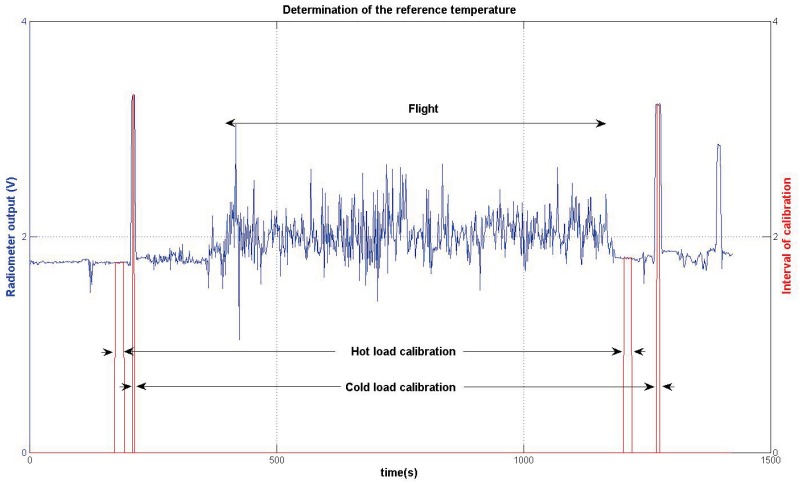

(b)

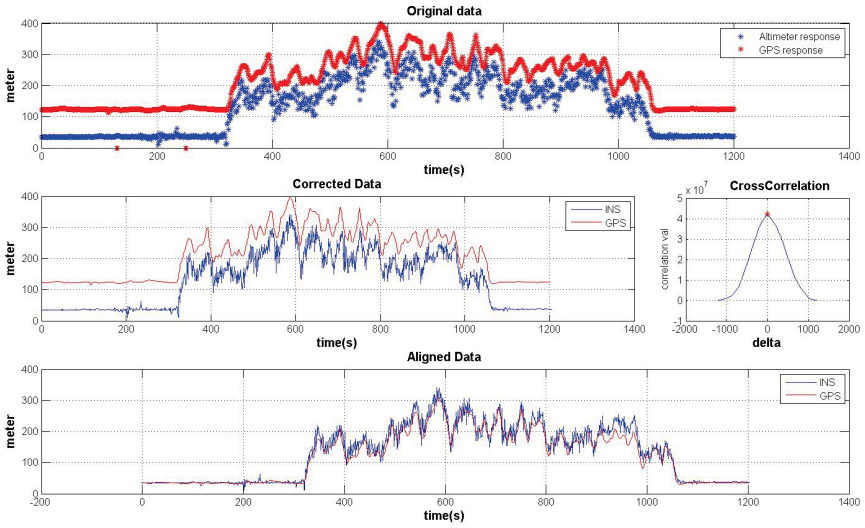

As shown in Figure 6a, histograms can also be plotted to detect relevant information, such as intervals of interest, and by extracting the desired ranges of antenna temperatures or aircraft height. Interesting parameters to be displayed are the antenna temperature and soil moisture maps in time intervals. The flight trajectory can be illustrated together with the corresponding antenna footprints plotted along the ground track (Figure 6b). The processor includes attitude and altitude filters to limit the range of valid incidence angles, eliminate Sun glints at high banking angles, radio frequency interference (RFI) peaks, or potential recording errors of the dataloggers.

Figure 6. Images showing the kind of target present in the scene. Test performed in a coastal zone. **(a)** Histogram plot in which different targets and other signals could be distinguished during the measurement: soil, water, calibration, and sun glints. **(b)** Trajectory plot of the flight superimposed with brightness temperatures.

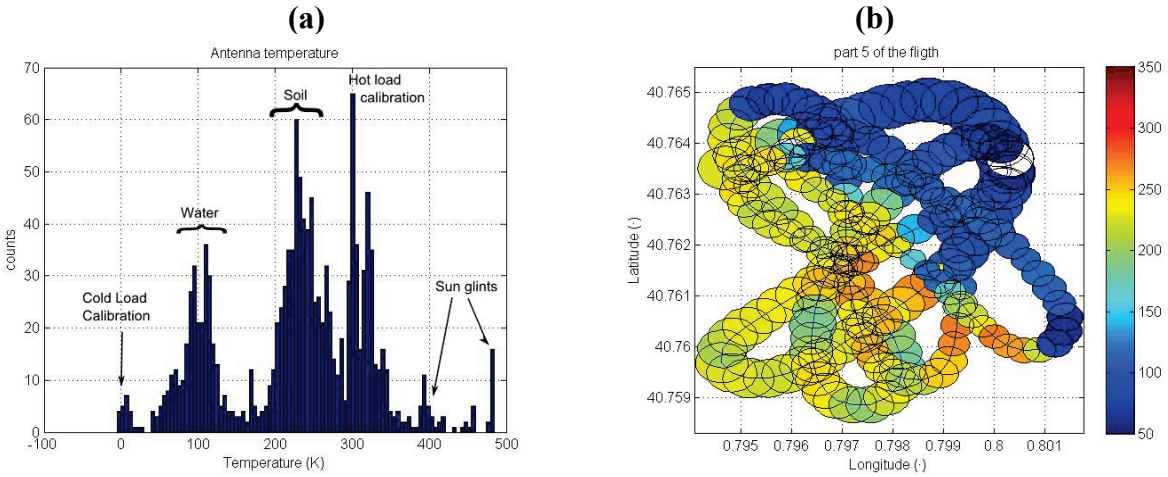

Finally, in order to fully cover a specific area (typically 1 km × 1 km) with the UAV flying at low altitudes (under 300 m), the flight plan is designed in such a way that several overpasses at different heights (*i.e.*, with different spatial resolutions) are obtained. In order to merge all the collected information, each footprint has to be properly weighted with the antenna's radiation pattern. Therefore, interpolation techniques have been developed to obtain images with soil moisture or antenna temperature information (Section 4.1.3). These images are then geo-referenced and linked to a map using Keyhole-Mark-up-Language (KML) [11] files that can be superimposed on Google Earth maps for a better interpretation.

4.1. Algorithm Description and Procedures

The soil moisture retrieval algorithm proceeds as follows:

- Raw data resampling.
- Radiometric calibration.
- Ground projection of the antenna footprint, taking into account the attitude and position of the platform.
- Spatial interpolation.
- Soil moisture retrieval.

The algorithm is described step by step in the following sections.

4.1.1. Data Resampling

GPS' largest errors are in the vertical direction. A barometric sensor is used to correct this information, and to refer all heights to ground level, so as to properly compute the antenna footprints. In order to geo-reference the radiometric data, it is necessary to synchronize the barometric altimeter, the GPS, and the radiometric data, since they are acquired at different sampling frequencies and by

different dataloggers. The altitude is referenced to the ground's altitude in order to properly compute the antenna footprints.

4.1.2. Radiometric Calibration

The radiometer's raw-data are converted into antenna temperatures through the radiometric calibration. In a Dicke radiometer, the relationship between its output voltage, v_o, and the antenna temperature can be expressed as [10]:

$$v_o = a(T_{REF} - T_A) + b \tag{3}$$

where T_{REF} is the temperature of the reference load (measured with a thermometer), T_A is the antenna temperature, and a and b are gain and offset constants to be determined during the absolute calibration with the hot-cold method [12]. A thermally isolated microwave absorber placed just in front of the antenna is used as a hot load, and pointing the antenna to the sky gives the equivalent of a cold load.

In case of temperature drifts during the flight, a linear behavior between two hot or cold load calibrations performed just before and after the flight, is assumed. In this case, the calibrations parameters can be determined as follows:

$$a(t) = a_b + \frac{a_f - a_b}{t_f - t_b}(t - t_b) \tag{4a}$$

and

$$b(t) = b_b + \frac{b_f - b_b}{t_f - t_b}(t - t_b) \tag{4b}$$

where t is the time and the subscripts b and f mean before and after the flight.

Finally, the time dependent coefficients $a(t)$ and $b(t)$ are used with T_{REF} to compute the calibrated antenna temperature at each sample. In case of the failure of all calibrations, a laboratory calibration with constant coefficients measured in the anechoic chamber can be used. For an integration time of τ = 100 ms, the measured calibration standards have standard deviations of σ_{hot} = 0.0045 V and σ_{cold} = 0.0052 V, which translate into sensitivities of ΔT_{hot} = 0.84 K and ΔT_{cold} = 1.22 K; these values are in agreement with theoretical predictions (Section 3).

4.1.3. Data Merging and Spatial Interpolation

Once the flight trajectory has been determined, the ground projection is performed and the footprint size and shape are determined. Then, the radiometric data has to be properly processed in order to obtain a geocoded SM map that can be linked to a KML file; to be finally overlaid with Google Earth maps. As described before, the data sampling rate is $f_s = 50$ Hz, and the UAV speed is $v_{UAV} \approx 40 m/s$. This means that the aircraft has moved 0.8 m between consecutive samples. If an average footprint of 100 m is considered, the pixels have a high-level of overlap, and thus, data must be properly interpolated.

For geo-statistical applications, the Kriging method [13] provides the optimal interpolator. It assigns weights according to a data-driven weighting function (spatial covariance values obtained through a semivariogram). However, for simplicity and computational speed considerations, the

algorithm performs an alternative method of assigning a weight to each footprint according to the modified two-dimensional (bivariate) Gaussian density function (*GDF*) that best fits the antenna pattern mainlobe. Each GDF has been adjusted to ensure that for the 3dB antenna footprint contour, the GDF value falls to the half of the maximum (−3 dB in antenna terms).

Finally, the resulting pixel is the product of a merge of all values from the footprints that intersect a given pixel. Every temperature value of the pixel is obtained from a weighted average of the different looks:

$$\hat{Z}_i = \frac{\sum_{k=1}^{n} GDF_k(d_k) \cdot Z_k}{\sum_{k=1}^{n} GDF_k(d_k)}, \tag{5}$$

where Z_k is the value of the k^{th} contributing antenna footprint, $\hat{Z}_i$ is the estimated value for the pixel i^{th}, d_k is the distance from the center of the pixel to the center of the k^{th} contributing antenna footprint, GDF_k is the *GDF* of the k^{th} contributing antenna footprint, and n is the total number of contributing footprints.

In this procedure, the footprints generated at lower altitudes will have a higher influence on the obtained pixel. In addition, to ensure nadir look observations, only footprints with incidence angles lower or equal to 10° are computed in the process. This will be further explained in the following section.

4.2. Soil Moisture Retrieval

The brightness temperature of the surface is measured by an antenna far away. In this case, the apparent temperature, T_{AP}, is the key parameter that depends on the brightness temperature of the surface under observation (T_B), the atmospheric upward radiation (T_{UP}), the atmospheric downward radiation scattered and reflected by the surface (T_{SC}), and the atmospheric attenuation (L_a). The downward radiation is mainly generated by the cosmic radiation level of the sky T≈ 2.7 K at L -band, and the downwelling atmospheric contribution, T_{DNatm} ≈ 2.1 K, at zenith. These values are fairly constant and will not affect the quality of the measurement, and are thus usually ignored. Since $T_{UP} \approx 0$ at low altitudes, T_{SC} is much smaller than the required accuracy and $L_a \approx 1$ (for $\theta = 0°$), at low altitudes, the apparent temperature T_{AP} at L-band can be approximated by the temperature emitted by the surface (T_B) weighted by the antenna pattern.

$$T_A = \frac{1}{\Omega_p} \iint_{4\pi} T_{AP}(\theta,\phi) \left| F_n(\theta,\phi) \right|^2 d\Omega, \tag{6}$$

where $F_n(\theta,\phi)$ is the normalized antenna voltage pattern, Ω_p is the equivalent antenna beam solid angle, and θ is the incidence angle.

The brightness temperature T_B of a soil covered by vegetation is usually estimated as the contribution of three terms: (i) the radiation from the soil that is attenuated by the overlying vegetation, (ii) the upward radiation from the vegetation, and (iii) the downward radiation from the vegetation, reflected by the soil, and attenuated by the canopy [12]:

$$T_{Bp}^{\text{model}} = \left(1 + \frac{1 - e_{bs}}{L_{veg}}\right)\left(1 - \frac{1}{L_{veg}}\right)(1 - \omega)T_{veg} + \frac{e_{bs}}{L_{veg}}T_{soil}, \tag{7}$$

where $e_{bs} = \left(1 - \Gamma^p\right)$ is the bare soil emissivity, Γ is the reflection coefficient, p is the polarization, T_{veg} and T_{soil} are the physical temperatures of the vegetation and soil, respectively, $L_{veg} = \exp(\tau \cdot \sec\theta)$ [Np] is the attenuation due to the vegetation cover, $\tau = b \times VWC$ is the optical thickness, b [m^2/kg] is a vegetation dependent factor [14], VWC is the vegetation water content [kg/m^2], and ω is the single scattering albedo. This formulation is known as the τ-ω model [14] and is based on the single scattering approach proposed in [15].

In the case of bare soil: $\tau = 0$, $L_{veg} \approx 1$, and $\omega = 0$ and (7) reduces to

$$T_B^p(\theta) = \left(1 - \Gamma^p(\theta)\right)T_{soil} \tag{8}$$

where the reflection coefficient at the air-ground interface $\Gamma^p(\theta)$ is computed using the Wang model [16] as:

$$\Gamma^p(\theta) = \left[\left(1 - Q_s\right) \cdot \Gamma^{spec,p}(\theta) + Q_s \cdot \Gamma^{spec,q}(\theta)\right] \cdot \exp\left(-h_s \cos^n\theta\right), \tag{9}$$

where Q_s is the mixing polarization parameter, and h_s is the surface roughness. Both are functions of the frequency. Recent studies have shown that h_s also depends on soil moisture [17]. In order to retrieve soil moisture from the antenna temperature at a single direction, some assumptions are made:

- The soil is bare and smooth (surface roughness parameter $h_s = 0$).
- Only incidence angles smaller than 10° have been retained, since the angular dependence of T_B around 0° is weak.

To determine the impact of the incidence angle, the emissivity of a bare flat soil is plotted *versus* soil moisture for three different incidence angles (θ = 0°, 10°, and 30°; Figure 7a). It could be seen that for incidence angles of up to 10°, the error is smaller than 1% compared with a 0° incidence. For incidence angles up to 30°, the error rises to 6%. In Figure 7b, the impact of vegetation cover is illustrated, showing the emissivity of soil *versus* SM for two different kinds of soils: bare soil and wheat. Compared with a bare soil, the error is 6% for 22 cm height vegetation and 15% for 60 cm vegetation. These values are obtained with an incidence angle of θ = 0°.

In order to speed up the retrieval process, an emissivity look-up table has been created with SM entries. The scattered radiation is also included for average soil moisture conditions [12]. Then, for a given T_{ph} and T_A, the SM is readily estimated.

Figure 7. Emissivity as a function of SM for **(a)** a bare flat soil *versus* SM at three different angles (θ = 0°, 10°, and 30°). The error compared with a θ = 0° is: 1% at θ =10°, and 6% at θ =30°, **(b)** for two different kind of soils: bare soil and pasture. The error is: 6% for 22 cm height vegetation and 15% for 60 cm height vegetation at θ = 0°.

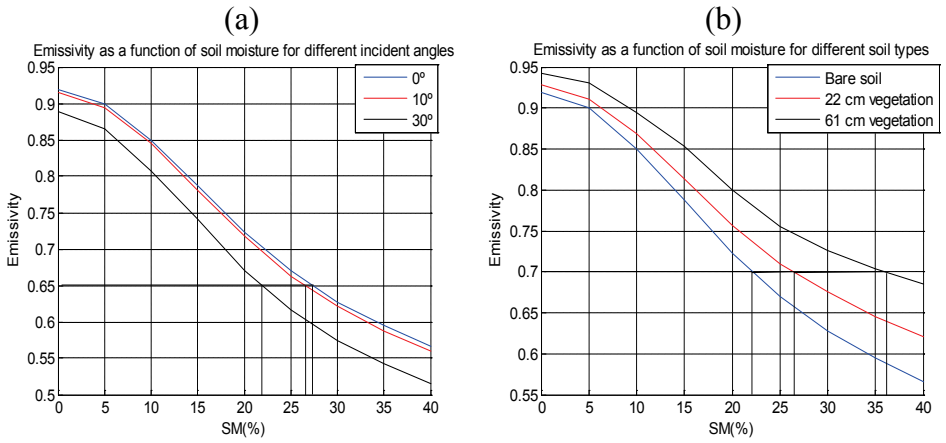

5. Experimental Results

Three experimental field campaigns have been conducted over different scenarios to retrieve soil moisture maps. The selected scenarios were:

(1) Ripollet site surroundings (Barcelona, Spain), used for agricultural applications: land and crop monitoring, with different irrigation levels,

(2) Ebro River mouth (Deltebre, Spain), not presented in this work, used for agricultural (rice fields) and coastal applications [18], and

(3) REMEDHUS site (Salamanca, Spain), used for SMOS calibration and validation (CAL/VAL) activities [19].

5.1. Soil Moisture Measurements at Ripollet Site Surroundings

The Ripollet site surroundings were chosen because the region has a radio control model flying club near agricultural fields. These fields showed interesting changes in soil moisture during the first half of 2009 due to the different irrigation levels during winter and spring. A measured soil moisture map from the Ripollet field is displayed in Figure 8a. The flight corresponds to April 29 (day of year (DoY) = 119), 2009. *In situ* ground truth measurements were taken with a moisture sensor ECH$_2$O EC-5 [20] at a vertical depth of 5 cm. Measurements were performed and two samples averaged. The positions of the soil moisture measurements were geo-coded using a commercial GPS receiver. The soil moisture ground truth (SM-GT) map was spatially interpolated with the same pixel resolution of the retrieved SM map and is shown in Figure 8b.

Figure 8. Experimental results of the Ripollet site surroundings, April 29 (DoY=119), 2009. Google Earth image size 1.5 km × 1 km. **(a)** Soil moisture map of Ripollet agricultural fields. **(b)** Ground truth soil moisture map of Ripollet.

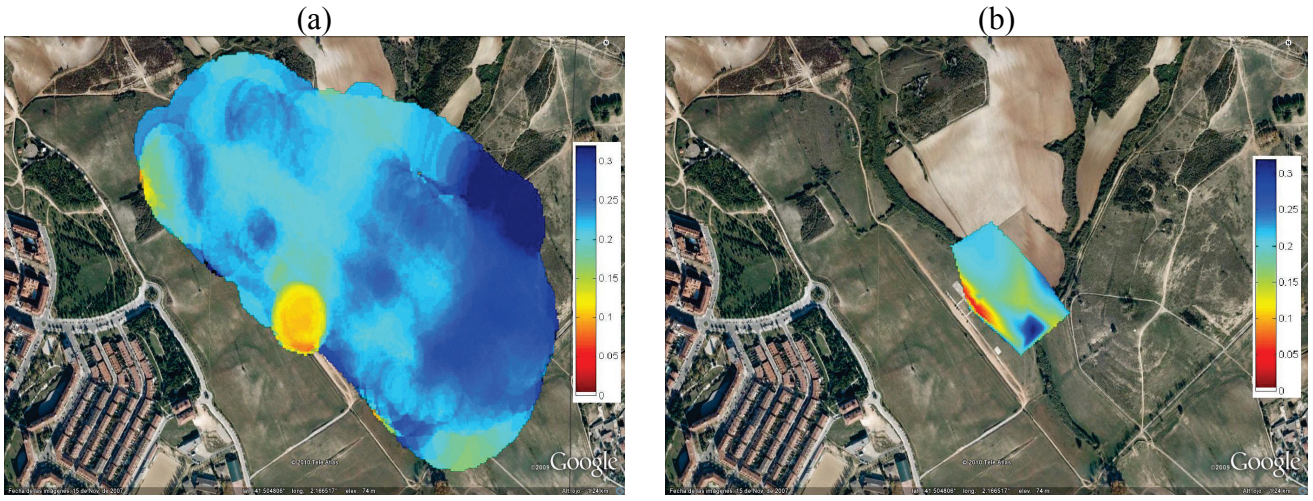

Figure 9 shows an error map of the retrieved soil moisture with ARIEL *versus* the ground truth measurements. In the upper left part of the error image, the absolute value varies from 6% to 9%. In this zone there is a hill with a 10% slope covered by dense wheat fields. In the center of the image, the error reaches 1%. There are two noticeable regions (shown in red) where the error reaches up to 16%. One region corresponds to the aircraft runway made of concrete, and the other is covered by tall vegetation (3 m height cane).

Figure 9. Retrieved soil moisture error map with ARIEL compared to ground truth measurements. In the center of the image, the absolute error reaches 1% and rises up to 9% in the upper left (data cursor value is 8.27%). Two noticeable zones (red and yellow), where the error reaches up to 16%, are the runway and a tall vegetation area (3 m height cane).

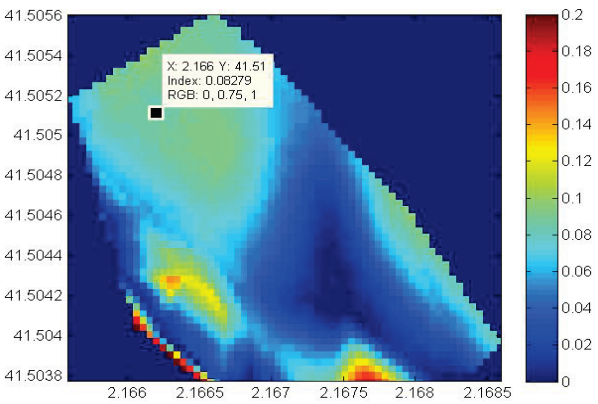

5.2. Soil Moisture Retrieval Tests at the Remedhus, SMOS Cal/Val Site Zamora, Spain

GRAJO (GPS and Radiometric Joint Observations) is a joint initiative between UPC and the Centro Hispano Luso de Investigaciones Agrarias (CIALE)/Universidad de Salamanca (USAL). The CIALE

group is in charge of the *in situ* measurements using TDR and Hydra Probes automatic sensors [21] in order to obtain, simultaneously, soil moisture and temperature at 5, 25, and 50 cm depths. UPC is in charge of the radiometric and the GPS reflectometer data acquisitions.

The GRAJO field campaigns in support to the SMOS calibration or validation have been carried out in Vadillo de la Guareña, Zamora, Spain from November 2008 until May 2010 [19].

The objectives of GRAJO are threefold:

- To validate and calibrate the SMOS-derived soil moisture map, at SMOS pixel-size levels.
- To study the variability of soil moisture within the SMOS footprint.
- To test pixel disaggregation techniques development in order to improve the spatial resolution of SMOS observations. These algorithms have been tested using airborne radiometric measurements over REMEDHUS acquired with the ARIEL radiometer.

The experiment with ARIEL at the REMEDHUS test site was planned to be performed over this very heterogeneous area, where the measured SM has variations from 2 to 50% in a 2 km^2 area. These conditions allowed one to validate the SM retrieval algorithm over those different kinds of terrains and SM values. The method's feasibility could be tested thanks to the information from a ground-truth SM map provided by CIALE.

Figure 10 shows a land use map of the area where four kinds of soil can be distinguished: cereal, vineyard, human-made buildings, and rangeland. There are also rural ways, trees, and a creek. This kind of land use implies a high degree of variability of the SM with abrupt changes.

Figure 10. Land use map for the experiment in Vadillo de la Guareña (Zamora, Spain).

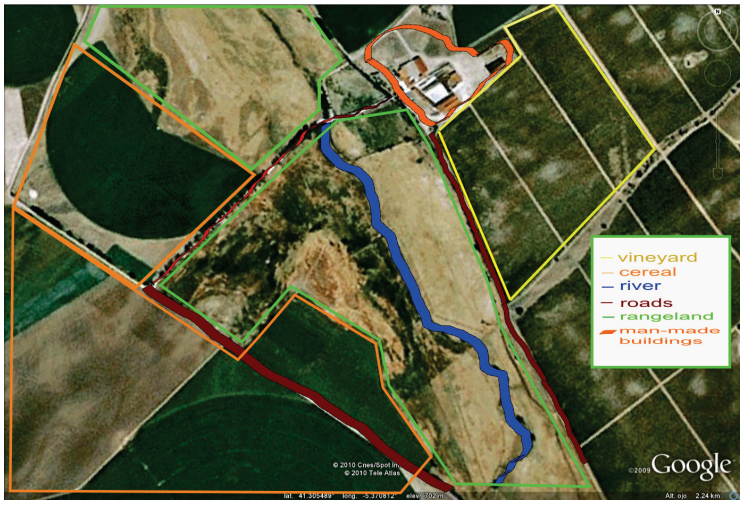

Flight measurements were carried out in the morning right after sunrise and in the evening right before sunset in order to reduce the effect of Sun interferences (due to reflections over the terrain). The retrieved soil moisture maps from the two flights are plotted in Figure 11a. Figure 11b shows the soil moisture ground truth map obtained by the CIALE/USAL team, which has been generated using Kriging interpolation techniques. The ground truth maps show variations in SM from 2% to almost 50%.

Figure 11. Experimental measurements in Vadillo de la Guareña (Zamora, Spain), March 25 (DoY = 84), 2009. **(a)** Soil moisture map mixing two different flights (square area of 2.28 km^2). Flight 1 covers the right image part and flight 2, the left one. **(b)** Ground-truth soil moisture map provided by CIALE/USAL.

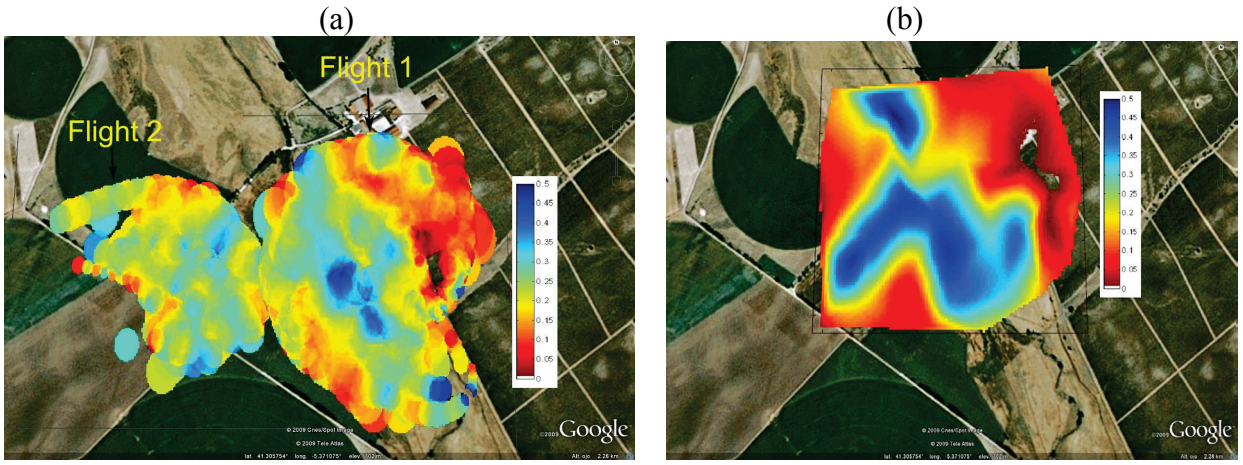

Since the experiment was carried out in a very heterogeneous area, the most homogeneous zones with lower variations in the SM (up to 15%) are analyzed first. Figure 12a shows the error map between the retrieved SM map from flight 1 (Figure 11a) and the ground truth measurements (Figure 11b) of part of the scenario (center of Figure 11a). The ground truth showed a variation of SM from 25 to 40%, and the obtained error map (difference between retrieved SM and ground truth in %) goes from 1 to 6%. The same results are obtained in other parts of the scenario. Figure 12b shows the error map of the left part of the scenario with information retrieved from second flight. The same results are obtained in this flight.

Figure 12. Error maps for the homogeneous zone from the retrieved SM *versus* ground truth measurements of **(a)** flight 1, and **(b)** flight 2.

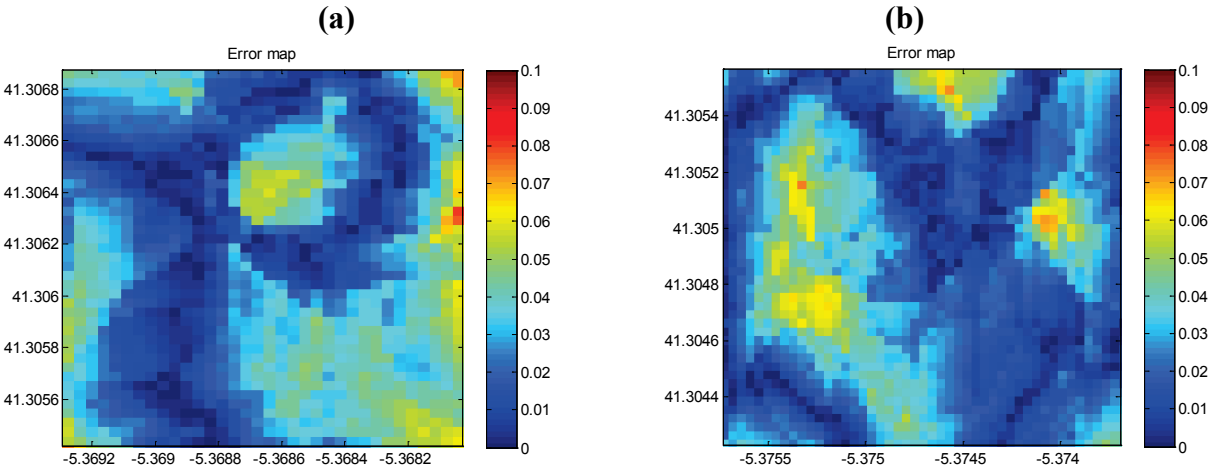

Figure 13a shows the error map in the complete image. It is easy to see that this absolute error increases at the corners of the area from 12% up to 20% due to the substantial reduction in the number of overpasses. It must be pointed out that some areas showed variations in SM from 4% to 46% at

distances closer than 70 m. These areas have been interpolated by the radiometer if a footprint of 100 m is observed that implies a large error in the retrieved SM value.

Figure 13b represents the error map in the complete image from the second flight. There are two zones in the center of the image where the error reaches 20%, for which some considerations must be taken into account. The flight was performed in the afternoon, and the ground truth map was taken in the morning simultaneously with the first flight so that in this zone, the variability in SM is higher due to the drying. One limitation of generating ground truth maps with interpolation methods is the variability of SM values in short distances. A source of error in the ground truth information is that of the accuracy of the sensor, which in this case is 1.5% [21].

Figure 13. Error maps for the full areas from retrieved SM *versus* ground truth measurements of **(a)** flight 1, and **(b)** flight 2. The dark blue points show the locations of the ground truth measurements.

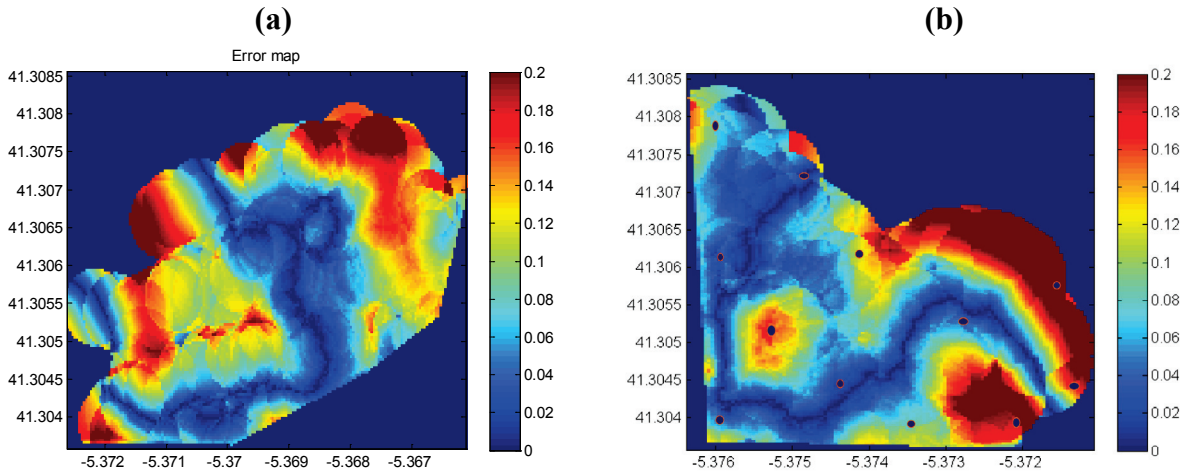

To better understand these large differences, biophysical parameters of the vegetation present in the site are provided in Table 1. The VWC was determined during the measurement, and the normalized difference vegetation index (NDVI) was measured with a USB4000 miniature fiber optic spectrometer from ocean optics.

Table 1. Biophysical parameters of the vegetation present in Vadillo de la Guareña (Zamora, Spain), March 25 (DoY = 84), 2009.

	NDVI	Growing Cycle	VWC (%)	FVC (%)
Grass/Pasture	0.60 to 0.85	Development	66 to 78	55 to 75
Barley/Cereal	0.63 to 0.72	Development	70 to 75	49 to 61
Vineyard	−0.01 to 0	Dormancy	--	--
Unproductive	−0.05 to 0	--	--	--

Based on Table 1 information, and on the land use map of Figure 10, the best results in the first flight were obtained over unproductive areas (bare soil or poor vegetation). The average errors were obtained over grass or pasture zones where higher vegetation indices were present.

The largest errors are obtained in the vineyard area. Despite its low vegetation index and poor water content, this area has a particular orography, with a 10% slope and a road (without ground truth information) that separates a very dense grass zone from the vineyard. Furthermore, this part of the scenario was not well covered during the flight; thus, few footprints contributed to the pixels.

In the second flight, the biggest errors are present over cereal zones where a high vegetation index is present. The same performance occurs over the roads where it is not possible to have ground truth information.

Other noticeable artifact in the image of Figure 11a is an apparent circular feature of the SM retrieved maps. It occurs in the zones where few over flights were performed, which means that few samples contribute to the pixel generation and the antenna footprint is depicted.

6. Conclusions

This work has presented the design and development of an airborne light weight radiometer at L-band (ARIEL). It also presents the software processor that includes different calibration techniques and interpolation and merging techniques. These techniques allow immediate processing of the data just at the end of the flight.

The flexibility of the UAV system has been applied for soil moisture mapping in cereal and vineyard fields located in the REMEDHUS SMOS CAL/VAL site. Results show that geo-referenced Google Earth maps of soil moisture and brightness temperature maps were obtained with estimated absolute errors between 1% and 6%. These results were obtained at homogeneous zones in agricultural fields.

The experimental tests planned in heterogeneous and vegetation covered soils show large errors where abrupt changes in SM are present and Krigging interpolation is prone to larger errors. The best results are obtained over more homogeneous zones, and the best image quality is achieved over the zones in which more overflights were performed.

Some improvements on the system are planned in order to increase the resolution. Also, a unique GPS-IMU unit will be included to avoid data resampling.

Acknowledgements

This project has been supported by the projects: MIDAS-5 ESP2007-65667-C04-02 and AYA 2008-05906-C02-01/ESP, TEC 2005.

This project has been supported by a grant of Universitat Politècnica de Catalunya, UPC Pre-PhD Scholarships.

This work, conducted as part of the award “Passive Advanced Unit (PAU): A Hybrid L-band Radiometer, GNSS-Reflectometer and IR-Radiometer for Passive Remote Sensing of the Ocean” made under the European Heads of Research Councils and European Science Foundation EURYI (European Young Investigator) Awards scheme in 2004, was supported by funds from the Participating Organizations of EURYI and the EC Sixth Framework Program.

References

1. Kerr, Y.H.; Waldteufel, P.; Wigneron, J.; Martinuzzi, J.; Font, J.; Berger, M. Soil moisture retrieval from space: the Soil Moisture and Ocean Salinity (SMOS) mission. *IEEE Trans. Geosci. Remote Sens.* **2001**, *39*, 1729-1735.
2. Lagerloef, G.; LeVine, D.; Chao, Y.; Colomb, R. Aquarius/SAC-D Mission; A key to understanding the links between salinity and climate variability. OS43C-02; AGU-ASLO Ocean Sciences, OS43C-02, February 2005.
3. Le Vine, D.M.; Lagerloef, G.S.E.; Colomb, F.R.; Yueh, S.H.; Pellerano, F.A. Aquarius: An instrument to monitor sea surface salinity from space. *IEEE Trans. Geosci. Remote Sens.* **2007**, *45*, 2040-2050.
4. Committee on Earth Science and Applications from Space: A Community Assessment and Strategy for the Future, National Research Council. Earth Science and Applications from Space: National Imperatives for the Next Decade and Beyond, 2007. Available online: http://www.nap.edu (accessed on 12 May 2010).
5. Miller, J.L.; Goodberlet, M.A.; Zaitzeff, J.B. Airborne salinity mapper makes debut in coastal zone. *Trans. American Geophysical Union EOS* **1998**, *79*, 173-177.
6. Haarbrink, R.; Shutko, A. New airborne sensor for soil moisture mapping. In *Proceedings of the Second International Workshop on The Future of Remote Sensing*, ISPRS Inter-Commission WG I/V, Autonomous Navigation, VITO/ISPRS, Antwerp, Belgium, October 2006.
7. McIntyre, E.M.; Gasiewski, A.J.; Leuski, V. Development of a lobe-differencing correlation radiometer (LDCR) for airborne UAV SSS mapping. In *Proceedings of the IEEE International Geoscience and Remote Sensing Symposium 2007*, Barcelona, Spain, 2007; pp. 1095-1097.
8. Valencia, E.; Acevo, R.; Bosch-Lluis, X.; Aguasca, A.; Rodriguez-Alvarez, N.; Ramos-Perez, I.; Marchan-Hernandez, J.F.; Glenat, M.; Bou, F.; Camps, A. initial results of an airborne light-weight l-band radiometer. In *Proceedings of the IEEE International Geoscience and Remote Sensing Symposium 2008*, Boston, MA, USA, 2008; pp. II-1176-II-1179.
9. Remote sensing laboratory. Available online: http://www.tsc.upc.edu/rslab/index.php (accessed on 12 May 2010).
10. Skou, N.; Le Vine, D. *Microwave Radiometer Systems Design and Analysis*, 2nd ed.; Artech House, Inc.: Norwood, MA, USA, 2006; p. 222.
11. KML standard. Available online: http://www.opengeospatial.org/standards/kml/ (accessed on 12 May 2010).
12. Ulaby, FT.; Moore, R.K.; Fung, A.K. *Microwave Remote Sensing. Active and Passive Vol I. Fundamentals and Radiometry*, 1st ed.; Artech House: Norwood, MA, USA, 1981; p. 456.
13. Stein, A.; Van der Meer, F.; Gorte, B. *Spatial Statistics for Remote Sensing: Remote Sensing and Digital Image Processing*; Kluwer Academic Publishers: Dordrecht, The Netherlands, 1999; p. 300.
14. Van de Griend, A.A.; Wigneron, J. The b-factor as a function of frequency and canopy type at h-polarization. *IEEE Trans. Geosci. Remote Sens.* **2004**, *42*, 786-794.
15. Kirdiashev, K.P.; Chukhlantsev, A.A.; Shutko, A.M. Microwave radiation of the earth's surface in the presence of vegetation cover. *Radio Eng. Electron. Phys.* **1979**, *2*, 37-56.

16. Wang, J.R.; Schmugge, T.J. An empirical model for the complex dielectric permittivity of soils as a function of water content. *IEEE Trans. Geosci. Remote Sens.* **1980**, *18*, 288-296.
17. Escorihuela, M.J.; Kerr, Y.H.; de Rosnay, P.; Wigneron, J.; Calvet, J.; Lemaitre, F. A simple model of the bare soil microwave emission at l-band. *IEEE Trans. Geosci. Remote Sens.* **2007**, *45*, 1978-1987.
18. Acevo-Herrera, R.; Aguasca, A.; Bosch-Lluis, X.; Camps, A. On the Use of Compact L-band Dicke Radiometer (ARIEL) and UAV for Soil Moisture and Salinity Map Retrieval: 2008/2009 Field Experiments. In *Proceedings of the IEEE International Geoscience and Remote Sensing Symposium 2009*, Cape Town, South Africa, 2009; pp. IV729-IV732.
19. Monerris, A.; Rodriguez-Alvarez, N.; Vall-llossera, M.; Camps, A.; Piles, M.; Martinez-Fernandez, J.; Sanchez-Martin, N.; Perez-Gutierrez, C.; Baroncini-Turricchia, G.; Acevo, R.; Aguasca, A. The GPS and RAdiometric Joint Observations Experiment at the REMEDHUS Site (Zamora-Salamanca Region, Spain). In *Proceedings of the IEEE International Geoscience and Remote Sensing Symposium 2009*, Cape Town, South Africa, 2009; pp. III286-III289.
20. ECH2O Soil Moisture Sensor. Available online: http://www.decagon.com/ag_research/soil/ec5.php (accessed on 12 May 2010).
21. Stevens' Hydra Probe II Soil Moisture Sensor (SDI-12 / RS485). Available online: http://www.stevenswater.com/catalog/products/soil_sensors/datasheet/hydraprobeiidatasheetnewweb.pdf (accessed on 12 May 2010).